Arabian Journal of Chemistry 16 (2023) 105294

Contents lists available at ScienceDirect

Arabian Journal of Chemistry

journal homepage: www.sciencedirect.com

Original article

Synthesis, crystal structure investigation, Hirshfeld and DFT studies of newly synthesized dihydroisoquinoline derivatives

Youness El Bakri [a,*], Shaaban K. Mohamed [b,*], Atazaz Ahsin [c], Subramani Karthikeyan [d], Suzan Abuelhassan [d], Abdu E. Abdel-Rahman [d], Islam S. Marae [d], Etify A. Bakhite [e], Joel T. Mague [f], Rashad Al-Salahi [g]

[a] Department of Theoretical and Applied Chemistry, South Ural State University, Lenin Prospect 76, Chelyabinsk 454080, Russian Federation
[b] Chemistry and Environmental Division, Manchester Metropolitan University, Manchester M1 5GD, England
[c] Beijing National Laboratory for Molecular Sciences, Institute of Chemistry, Chinese Academy of Sciences, Beijing 100190, China, School of chemical sciences, University of Chinese Academy of Sciences, Beijing 100049, China
[d] Centre for Healthcare Advancement, Innovation and Research, Vellore Institute of Technology University, Chennai Campus, Chennai 600127, India
[e] Department of Chemistry, Faculty of Science, Assiut University, Assiut 71516, Egypt
[f] Department of Chemistry, Tulane University, New Orleans, LA 70118, USA
[g] Department of Pharmaceutical Chemistry, College of Pharmacy, King Saud University, Riyadh 11451, Saudi Arabia

ARTICLE INFO

Article history:
Received 16 April 2023
Accepted 20 September 2023
Available online 26 September 2023

Keywords:
Dihydroisoquinoline
Crystal structure
NBO
NLO
Molecular docking
ADMET

ABSTRACT

Isoquinoline and its derivatives, which constitute an important category of heterocyclic compounds and are found in a variety of naturally occurring alkaloids, serve a variety of biological purposes such as a potent agonist for human melatonin receptors 1. This research was conducted in an attempt to develop new dihydroisoquinoline molecules (**III** and **IV**). Single-crystal X-ray crystallography study validated their structures. The Hirshfeld surface analysis identifies intermolecular interactions by using a 2-D fingerprint map to recognize each type's relative contribution H···H connections are discovered to be dominating. The interaction energies between chemical pairs in crystal structures were found using an energy framework analysis. The DFT investigation demonstrates the electronic stability and reactivity of the compounds using the HOMO-LUMO and global reactivity descriptors, indicating that **IV** has higher chemical reactivity than **III**. The derived polarizability (αo) and hyperpolarizability (βo) values were used to calculate the optical and nonlinear optical characteristics of **III** and **IV**. The **IV**'s significant βo value (488.94 au) indicates that it has good optical and NLO qualities. Molecular docking simulation using human melatonin receptors 1 was used to better understand the binding interaction mechanism of the title compounds. In addition, ADMET evaluations were performed to establish the therapeutic potential of **III** and **IV**.

1. Introduction

The neuromodulator melatonin (MLT) regulates numerous aspects of the brain, including circadian rhythms, mood, pain, and sleep. Melatonin primarily modulates the MT1 and MT2 G-protein coupled receptors. Melatonin affects the MT1 (previously known as Mel1a or ML1A) and MT2 (previously known as Mel1b or ML1B) receptors (Dubocovich et al., 2010). The human melatonin receptors hMT1 and hMT2 have distinct molecular structures (Reppart et al., 1996), pharmacological properties (Audinot et al., 2003; Dubocovich et al., 2010; Reppart et al., 1996), and chromosomal locations (4q35.1 for MT1 and 11q21-q22 for MT2) (Al-Ghoul et al., 1998). The human MT1 and MT2 receptors have lengths of 350 and 362 nm and molecular masses of 39–40 kDa, respectively. They share 70% of their transmembrane domains and 55% of their overall amino acid sequences.

Forskolin suppresses forskolin-stimulated cAMP, protein kinase A signaling, and CREB phosphorylation when the MT1 melatonin receptor associates with the pertussis toxin-sensitive Gi and -insensitive Gq/11 G proteins. Moreover, the MT1 receptor

* Corresponding authors.
E-mail addresses: yns.elbakri@gmail.com (Y. El Bakri), shaabankamel@yahoo.com (S.K. Mohamed).

Peer review under responsibility of King Saud University.

Production and hosting by Elsevier

https://doi.org/10.1016/j.arabjc.2023.105294
1878-5352/

Table 1
Experimental data and refinement details.

Compound **CCDC deposit Number**	**III** **2209903**	**IV** **2242649**
Chemical formula	$C_{21}H_{20}N_2OS$	$C_{26}H_{23}N_3OS$
M_r	348.45	425.53
Crystal system, space group	Monoclinic, $P2_1/n$	Triclinic, *P-1*fx1
Temperature (K)	170	150
a, *b*, *c* (Å)	11.1145 (3), 13.7766 (3), 12.9339 (3)	8.8009 (6), 11.5653 (8), 11.8909 (8)
α, β, γ (°)	90, 94.722 (1), 90	68.324 (3), 87.083 (3), 75.382 (3)
V (Å^3)	1973.72 (8)	1087.12 (13)
Z	4	2
Radiation type	Mo *K*α	Mo *K*α
μ (mm^{-1})	0.17	0.17
Crystal size (mm)	0.37 × 0.29 × 0.19	0.35 × 0.27 × 0.07
Data collection		
T_{min}, T_{max}	0.85, 0.89	0.87, 0.91
No. of measured, independent and observed [$I > 2\sigma(I)$] reflections	94944, 5994, 5057	72323, 8104, 7245
R_{int}	0.045	0.025
$(\sin\theta/\lambda)_{max}$ (Å^{-1})	0.717	0.766
Refinement		
$R[F^2 > 2\sigma(F^2)]$, $wR(F^2)$, *S*	0.044, 0.145, 1.07	0.039, 0.103, 1.05
No. of reflections	5994	8104
No. of parameters	229	286
H-atom treatment	H-atom parameters constrained	H atoms treated by a mixture of independent and constrained refinement
$\Delta\rho_{max}$, $\Delta\rho_{min}$ (e Å^{-3})	0.44, −0.25	0.45, −0.26

enhances the activation of mitogen-activated protein kinase 1/2 and extracellular signal-regulated kinase 1/2, as well as potassium conductance through Kir inwardly rectifying channels.

Determining the pharmacology and function of melatonin receptors can be challenging because their natural binding site densities in animal tissues are low or undetectable, particularly for the MT2 receptor (Liu et al., 1997). Using receptor autoradiography with 2-[125I]-iodomelatonin, *in situ* mRNA hybridization methods, and immunohistochemistry, the MT1 and MT2 receptor sites have been mapped to distinct regions of the rat and human nervous systems, including the SCN, cerebellum, thalamus, and hippocampus, as well as peripheral tissues (Adamah-Biassi et al., 2014; Al-Ghoul et al., 1998; Mazzucchelli et al., 1996; Weaver et al., 1989). Prototype competitive melatonin receptor antago-

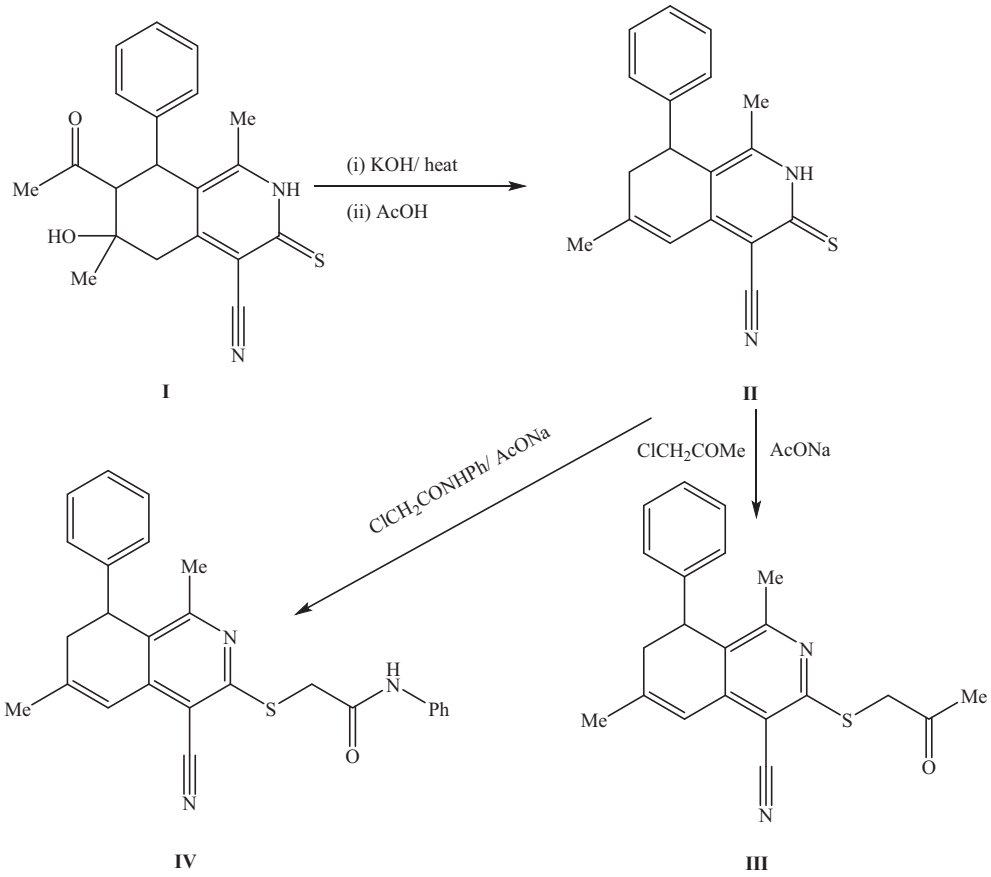

Scheme 1. Synthesis of compounds **III** and **IV.**

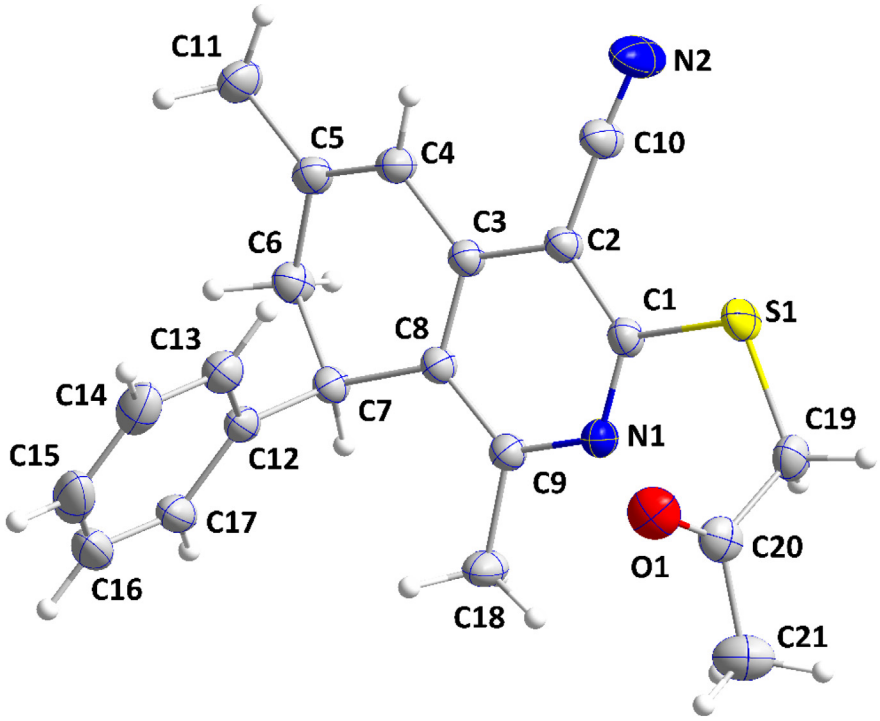

III

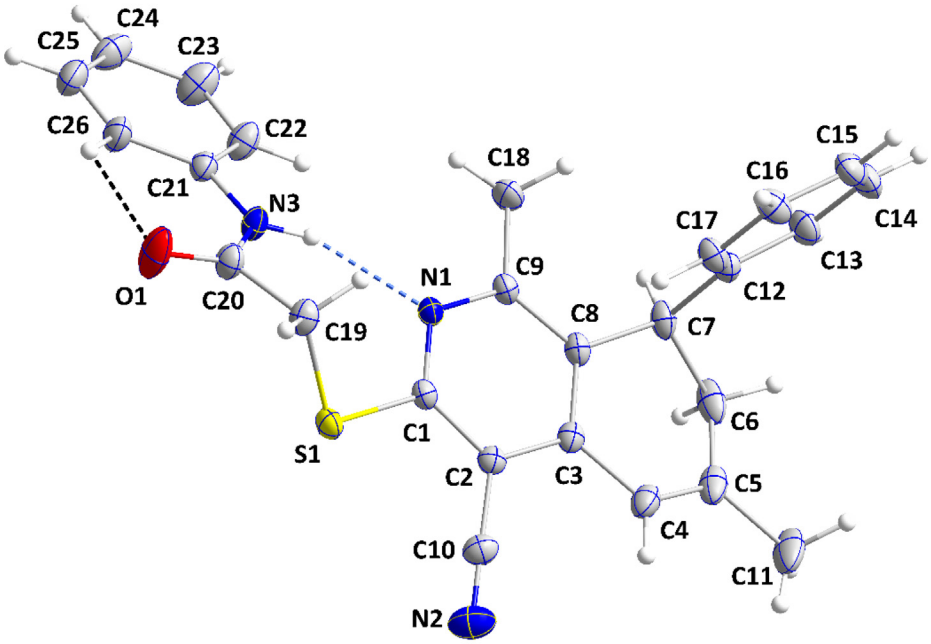

IV

Fig. 1. ORTEP diagram of compounds **III** and **IV.**

nists, such as luzindole and 4-phenyl-2-propionamidotetralin, were employed in pharmacological approaches or genetic deletion of the MT1 or MT2 melatonin receptor in mice (Al-Ghoul et al., 1998; Audinot et al., 2003; Dubocovich et al., 2010; Liu et al., 1997; Sherman et al., 2006b).

The biological and therapeutic properties of isoquinolines are of enormous significance to mankind (Scott and Williams, 2002). Particularly, 1,2-dihydroisoquinolines have sedative (Asghari et al., 2014), depressive (Lukevics et al., 1997), anticancer (Tietze et al., 2004), and antibacterial properties. Recently, NH-acids like indoles (Nassiri et al., 2008) and amides (Yavari et al., 2007) as well as CH-acids like phenyl acetylene (Yadav et al., 2008), β-diketones (Anary-Abbasinejad et al., 2010), and β-nitro ketones (Yavari et al., 2009), and OH-acids like 6-hydroxy1-benzofuran (Khaleghi et al., 2011) trapped the 1,4- dipolar intermediates produced by reacting isoquinoline with acetylenic esters. On the other hand, there has been a rise in interest in biological compounds that include kojic acid and 8-hydroxyquinoline. The bioactivities of kojic acid, 8-hydroxyquinoline, and its derivatives have been demonstrated to include antimicrobial (Shen et al., 1999), anticancer (Collery et al., 2000), antioxidant (Wehner et al., 1978), and antibacterial (Albert et al., 1947) properties.

Researchers have effectively discovered high-affinity and selective MT2 receptor ligands (Burley et al., 2021), while high-effectiveness selective MT1 receptor ligands have not been identified (Weaver et al., 1989). The MT1 selective ligands on the market are either partial agonists or antagonists with high selectivity for 2-[125I]-iodomelatonin binding to human recombinant MT1 receptors; however, in functional tests, this selectivity is substantially reduced (Mazzucchelli et al., 1996). Our new substances target the MT1 receptor, according to structural activity relationship studies, and we performed computational calculations to investigate their binding properties.

The theoretical investigation provides insight into the chemical reactivity and applicability of examined compounds for new purposes. DFT is the most practical theoretical technique for comprehending the structural reactivity and topological features of newly synthesized molecules. We focused on electrical characteristics, global reactivity descriptors, and optoelectronic properties of compounds in this endeavor. The optical and nonlinear optical (NLO) characteristics of dihydroisoquinoline derivatives are evaluated using the B3LYP (hybrid method) and the 6–31 + G(d,p) basis set. We conducted the complete simulation with Gaussian 09 and visualized it with the GaussView program.

Table 2
Hydrogen-bond geometry for 1 (Å,°) Cg3 is the centroid of the C12·C17 benzene ring.

D—H···*A*	*D*—H	H···*A*	*D*···*A*	*D*—H···*A*
C11—H11B···Cg3^{i}	0.98	2.93	3.9037(15)	175
C16—H16···N2^{ii}	0.95	2.53	3.352(2)	145
C19—H19B···N2^{iii}	0.99	2.42	3.3148(18)	151

Symmetry codes: (i) − x + 1/2, y − 1/2, −z + 1/2; (ii) − x + 1/2, y + 1/2, −z + 1/2; (iii) − x + 1/2, y + 1/2, −z + 3/2.

2. Instrument

2.1. Synthesis of compounds III and IV

Compound **II** (2.92 g, 0.01 mol), chloroacetone (0.01 mol) or *N*-aryl-2-chloroacetamide (0.01 mol), and sodium acetate trihydrate (1.50 g, 0.011 mol) were mixed in ethanol (60 mL) and heated under reflux for one hour before being allowed to stir at room temperature overnight. A colorless **III** or **IV** crystal was obtained by collecting the resulting solid and recrystallizing it from ethanol.

2.1.1. 3-(acetylmethylsulphenyl)-4-cyano-1,6-dimethyl-8-phenyl-7,8-dihydroisoquinoline (III)

Using chloroacetone as starting material; m.p.: 103–104 °C; yield: 93%. IR: 3067 (C–H, sp^2); 2976, 2921 (C–H, sp^3); 2215 (C≡N); 1728 (C = O, acetonyl), 1641 (C = N). ^{1}H NMR: 7.19–7.24 (m, 3H, Ar-H); 6.98–7.00 (d, *J* = 4, 2H, Ar-H); 6.62 (s, 1H, C^5H); 4.17–4.19 (d, *J* = 8, 1H, C^8H); 3.92–4.04 (dd, 2H, SCH_2); 2.93–3.00

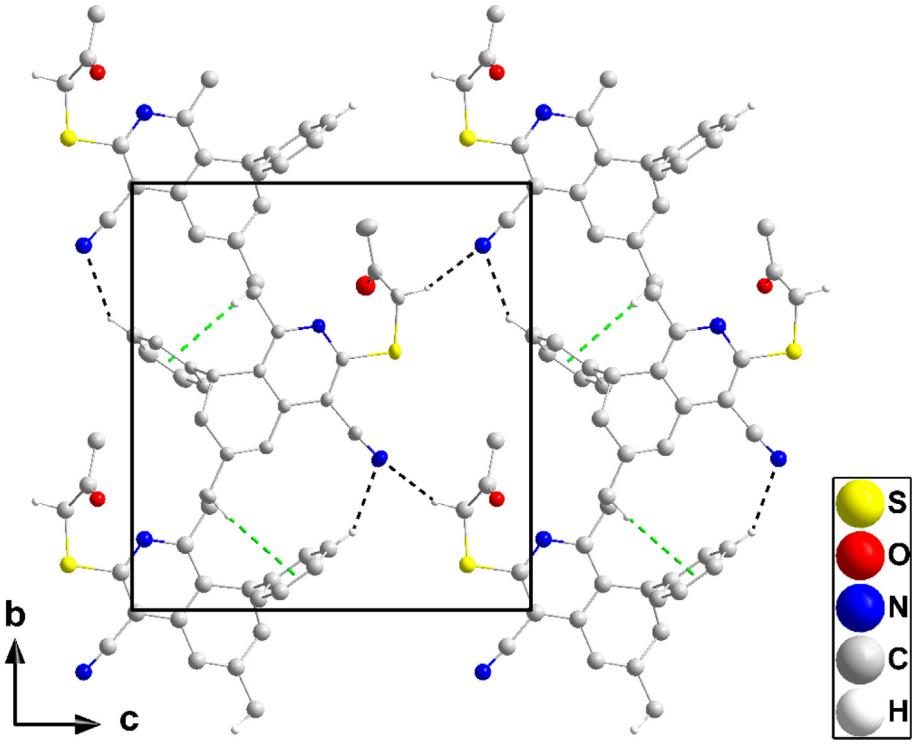

Fig. 2. A portion of one layer in **III** viewed along the *a*-axis direction with C—H···N hydrogen bonds and C—H···π (ring) interactions depicted, respectively, by blue and green dashed lines. Non-interacting hydrogen atoms are omitted for clarity.

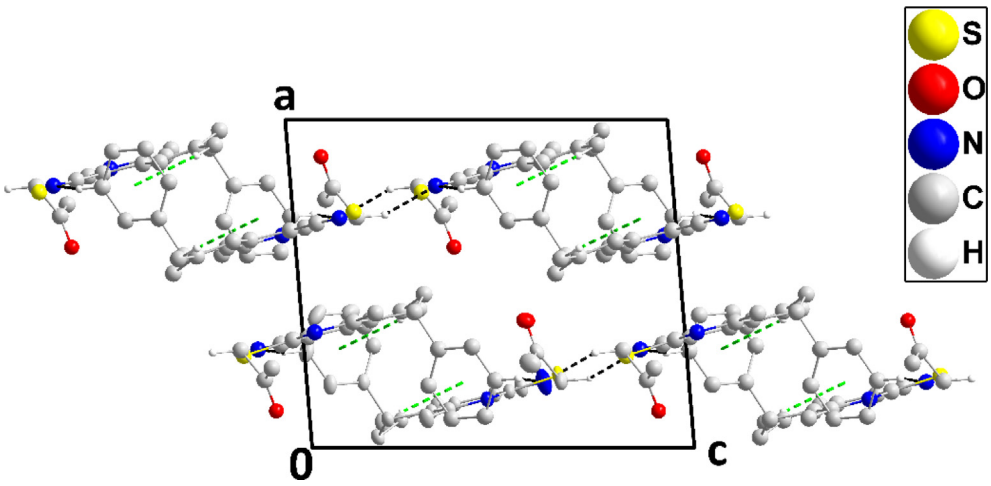

Fig. 3. Packing in **III** viewed along the *b*-axis direction with intermolecular interactions depicted as in Fig. 2. Non-interacting hydrogen atoms are omitted for clarity.

(dd, 1H, C^7H); 2.50–2.54 (d, 1H, C^7H); 2.33 (s, 3H, $COCH_3$); 2.28 (s, 3H, CH_3 at C-1); 1.88 (s, 3H, CH_3 at C-6) ppm. Anal. Calcd. for $C_{21}H_{20}N_2OS$ (348.13): C, 72.38; H, 5.79; N, 8.04; O, 4.59; S, 9.20%. Found: C, 71.99; H, 6.06; N, 8.35; O, 4.63; S, 8.94%.

Table 3
Hydrogen-bond geometry in 2 (Å,°) Cg3 and Cg4 are, respectively, the centroids of the C12···C17 and the C21···C26 benzene rings.

D—H···*A*	*D*—H	H···*A*	*D*···*A*	*D*—H···*A*
N3—H3···N1	0.902(9)	2.090(10)	2.9461(10)	158.0(13)
C7—H7···N2^{i}	1.00	2.41	3.3588(14)	157
C19—H19A···O1^{ii}	0.99	2.48	3.4657(12)	171
C19—H19B···Cg4^{iii}	0.99	2.74	3.5686(11)	142
C24—H24···Cg3^{iv}	0.95	2.67	3.4831(13)	144
C26—H26···O1	0.95	2.28	2.8929(14)	121

Symmetry codes: (i) x + 1, y, z; (ii) − x, −y + 2, −z + 1; (iii) − x + 1, −y + 2, −z + 1; (iv) ×, y + 1, z − 1.

2.1.2. 2-((4-cyano-1,6-dimethyl-8-phenyl-7,8-dihydroisoquinolin-3-yl)thio)-N-acetamide (IV)

Using *N*-phenyl-2-chloroacetamide as starting material; m.p.: 159–160 °C; yield: 4.3 g (84%). IR: 3297–3267(NH); 3060 (C–H, sp^2); 2923 (C–H, sp^3); 2220 (C≡N); 1679 (C = O); 1645 (C = N). ^{1}H NMR ($CDCl_3$): 9.47 (s, 1H, NH); 6.99–7.41 (m, 10*H*, ArH); 6.64 (s, 1H, C^5H); 4.21–4.23 (d, *J* = 10, IH, C^8H); 3.88–4.02 (dd, 2H, SCH_2); 2.96–3.01 (dd, 1H, C^7H); 2.52–2.56 (d, 1H, C^7H); 2.42 (s, 3H, CH_3); 1.90 (s, 3H, CH_3). ^{13}C NMR (126 MHz, DMSO d_6): δ 166.70, 159.66, 158.86, 149.18, 145.49, 142.97, 139.54, 129.20, 129.10, 127.51, 127.18, 124.96, 123.85, 119.75, 118.18, 115.55, 99.53, 37.93, 37.39, 35.47, 24.54, 22.51. Anal. Calcd. For $C_{26}H_{23}N_3$-

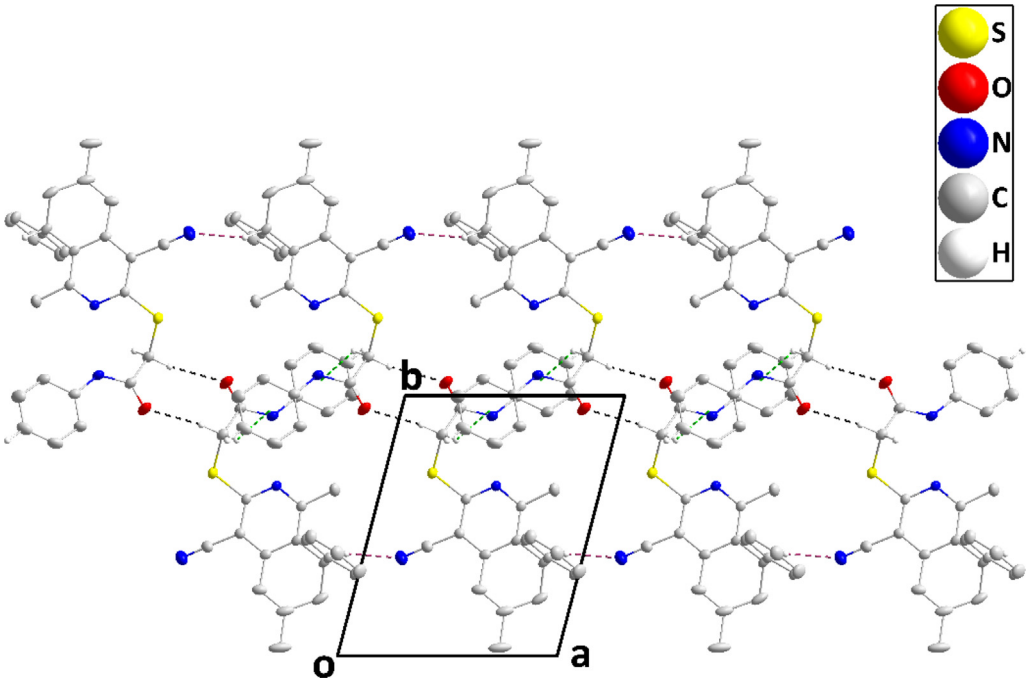

Fig. 4. A portion of one ribbon in **IV** viewed along the *c*-axis direction with C—H···O and C—H···N hydrogen bonds depicted, respectively, by black and purple dashed lines. The C—H···π(ring) interactions are depicted by green dashed lines.

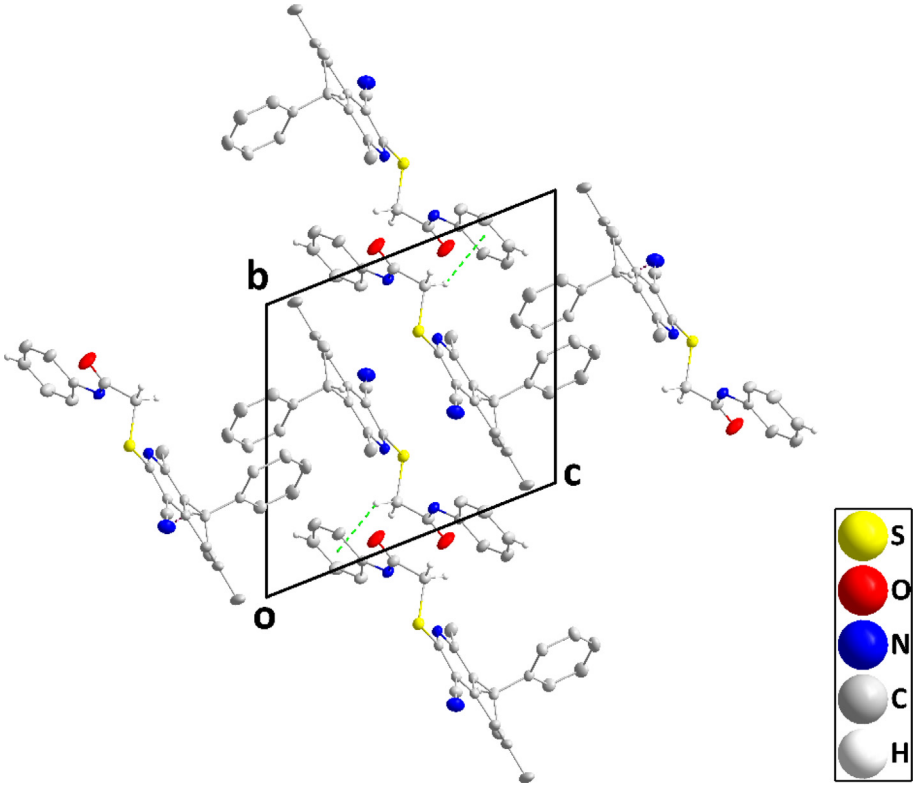

Fig. 5. Packing in **IV** viewed along the *a*-axis direction with intermolecular interactions depicted in Fig. 2.

OS (425.16): C, 73.38; H, 5.45; N, 9.87; O, 3.76; S, 7.53%. Found: C, 73.68; H, 5.32; N, 9.64O, 3.79; S, 7.57%.

2.2. X-ray crystallographic analysis

On a Bruker D-8 Quest PHOTON 3 diffractometer, crystals III and IV were mounted on polymer loops and deposited in a cold nitrogen stream. Under the control of the APEX4 software (Bruker (2016), 2016) intensity data were collected, and the raw intensities were converted to F^2 values using SAINT ("Saint. Data Reduction and Correction Program.Version 8.34A.Bruker AXS Inc., Madison, Wisconsin, USA, 2014," n.d.) which also conducted a global refinement of the unit cell parameters. Corrections for absorption and merging of equivalent reflections were carried out using SADABS, and the structures were solved using dual space techniques (SHELXT ("Bruker. APEX3, SADABS, SAINT and SHELXTL. Bruker AXS Inc., Madison, Wisconsin, USA", 2016)). The structures were refined utilizing full-matrix, least-squares techniques (SHELXS (Sheldrick, 2015)) with hydrogen atoms attached to carbon included as riding contributions in idealized positions and those attached to nitrogen in IV refined using the DFIX 0.91 0.01 instruction. Details about crystal and refinement are listed in Table 1.

2.3. Computational details

The theoretical reactivity indices generated from the conceptual Density Functional Theory (DFT) (Domingo et al., 2016) have been a significant help in the semiquantitative study of organic reactivity. DFT simulations were performed in Gaussian 09 (Caricato et al., 2009) to gain insight into the molecular reactivity and optical characteristics, and the geometry was visualized in GaussView 6.0 (Dennington et al., 2009). Every one of those DFT simulations was conducted with the B3LYP functional and the 6–31 + G(d,p) basis set. Using the B3LYP functional is in line with previously reported findings (Tirado-Rives and Jorgensen, 2008; Zhao and Truhlar, 2006) in the literature, so it was used for this investigation.

Table 4
Hirshfeld Surface Property Information (d_i and d_e in Å).

III			
	Minimum	Mean	Maximum
d_i (Å)	0.9828	1.7978	3.9652
d_e (Å)	0.9838	1.7985	3.7848
d_{norm}	−0.2248	0.6444	2.5839
Shape index	−0.9950	0.2150	0.9963
curvedness	−3.7834	−1.0015	0.4397
IV			
d_i (Å)	0.981	1.726	2.608
d_e (Å)	0.981	1.736	2.574
d_{norm}	−0.225	0.510	1.463
Shape index	−0.993	0.207	0.999
curvedness	−3.702	−1.016	0.256

Initially, frequency simulations were done to determine stability and thermochemical characteristics after the geometries of **III** and **IV** were optimized at the B3LYP level. Frontier molecular orbital (FMO) and NBO charge studies, as well as the ionization potential and electron affinity, were also performed. A density of states (DOS) analysis was also performed to obtain a fuller understanding of reactivity. For optical and NLO properties, the dipole moments (μ_o), polarizability (α_o), hyperpolarizability (β_o), and projection of hyperpolarizability on the dipole moment vector were determined with the same functionality.

Hirshfeld surface analysis was performed with the CrystalExplorer software (Spackman et al., 2021) to visualize the regions of the closest intermolecular interactions in the crystal and to determine the contribution of each specific type of interaction.

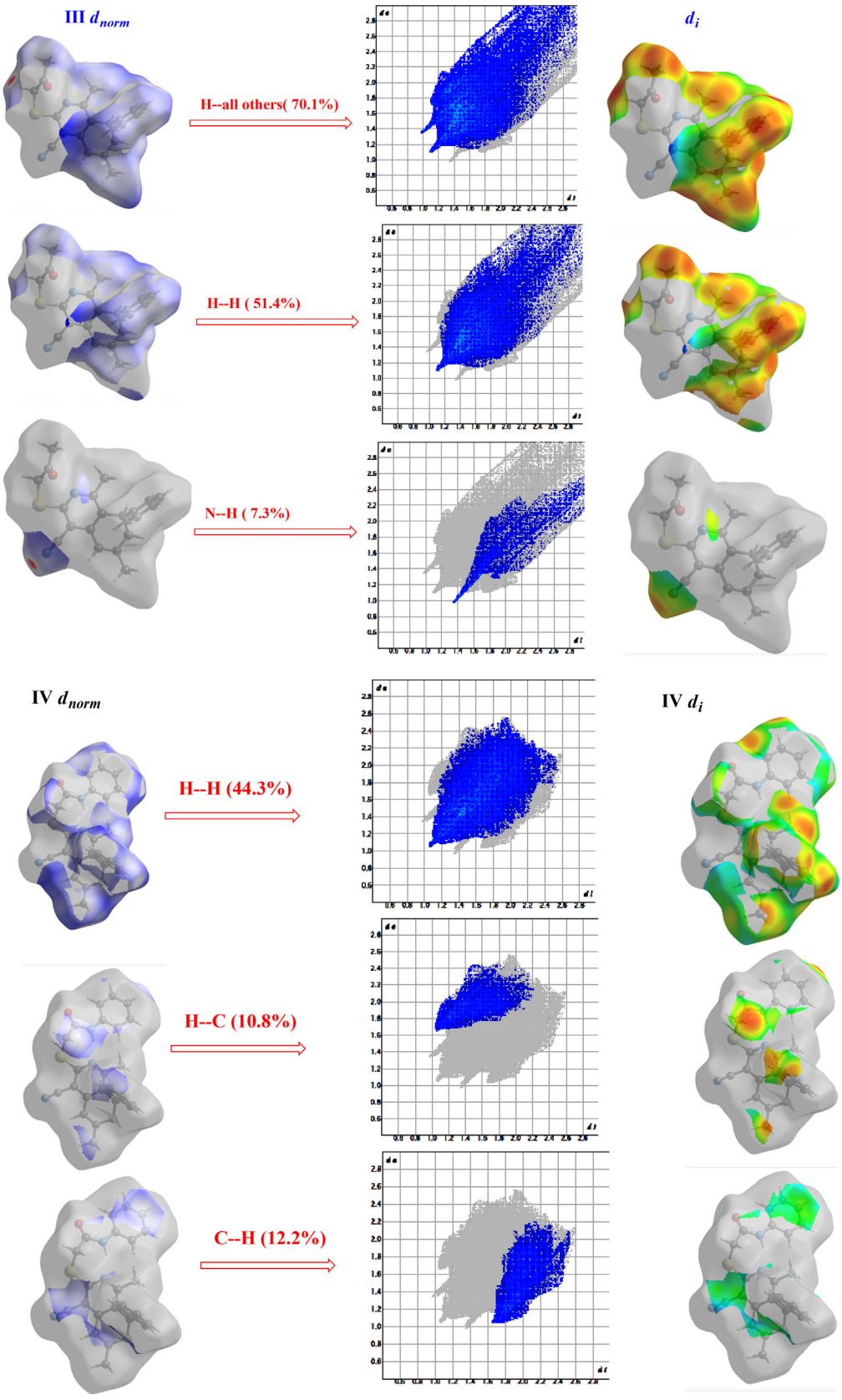

Fig. 6. 3D Hirshfeld surfaces with 2-D fingerprint plots for **III** and **IV.**

Table 5
Fingerprint plot results by element type; surface area included (as a percentage of the total surface area) for close contacts between atoms inside and outside the surface for **1II** and **IV.**

III					
Inside Atom	**Outside Atom**				
	S	**O**	**N**	**C**	**H**
C	0.2	0.1	0.6	3.2	7.0
H	2.1	5.7	5.6	5.3	51.4
N	–	–	0.1	0.6	7.3
O	–	–	–	–	6.4
S	–	–	–	0.2	4.2
IV					
Inside Atom	**Outside Atom**				
	S	**O**	**N**	**H**	**C**
C	0.6	–	1.1	12.2	4.0
H	2.4	3.6	5.6	44.3	10.8
N	–	–	0.2	6.1	1.1
O	–	–	–	4.0	–
S	–	–	–	3.5	0.6

2.4. Molecular docking and ADMET analysis

The crystal structure of the protein was extracted from the protein data bank (Burley et al., 2021) with PDB ID: 6ME2 (Stauch et al., 2019). Initially, the protein structure was pre-processed to remove crystal water molecules and het atoms followed by optimization and minimization of the structure with the OPLS2005 force field using the protein wizard panel in the Schrodinger package. Simultaneously, the ligand molecules **III** and **IV** and the native ligand molecule were energetically minimized and incorporated separately into the protein's native ligand site to interact. Molecular docking simulations were performed using the induced fit docking panel (Sherman et al., 2006b, 2006a) from the Schrodinger package. Finally, ADMET parameters analyses were carried out using the Swiss ADME(https://www.swissadme.ch/) and ProTox II (https://tox-new.charite.de/protox_II/index.php?site = compound_input) web server.

3. Results and discussion

3.1. Chemistry of compounds III and IV

As illustrated in Scheme 1, the 1,6-dimethyl-8-phenyl-3-thioxo-tetrahydroisoquinoline-4-carbonitrile (**II**) was allowed to react with chloroacetone or aryl-2-chloroacetamide in the presence of sodium acetate trihydrate in ethanol (60 mL). A colorless **III** or **IV** crystal was obtained by collecting the resulting solid and recrystallizing it from ethanol. The chemical structures of compounds **III** and **IV** were confirmed by NMR, IR, and elemental analysis techniques, and have been unambiguously proven by X-ray crystallography (Fig. 1). Thus, IR spectrum of compound **III** showed characteristic absorption bands at 3297–3267 cm^{-1} for (NH); 3060 cm^{-1} for (C–H, sp^2); 2923 cm^{-1} for (C–H, sp^3); 2220 cm^{-1} for (C≡N); 1679 cm^{-1} for (C = O); 1645 cm^{-1} for (C = N). ^{1}H NMR spectrum of compound **III** (DMSO d_6, 500 MHz) showed the following signals: a singlet at δ 9.47 (1H, NH); a multiplet at δ 6.99–7.41 (10*H*, ArH); a singlet at δ 6.64 (1H, C^5H); a doublet at δ 4.21–4.23 (J = 10, IH, C^8H); a double doublet at δ 3.88–4.02 (2H, SCH_2); a double doublet at δ 2.96–3.01 (1H, C^7H); a doublet at δ 2.52–2.56 (1H, C^7H); a singlet at δ 2.42 (3H, CH_3); a singlet at δ 1.90 (3H, CH_3) which are in agreement with its proposed structure. IR spectrum of compound **IV** showed characteristic absorption bands at 3067 cm^{-1} for (C–H, sp^2); 2976, 2921 cm^{-1} for (C–H, sp^3); 2215 cm^{-1} for (C≡N); 1728 cm^{-1} for (C = O, acetonyl), 1641 cm^{-1} for (C = N). ^{1}H NMR spectrum of compound **IV** ($CDCl_3$, 500 MHz) showed a multiplet at δ 7.19–7.24 (3H, Ar-H); a doublet at δ 6.98–7.00 (J = 5, 2H, Ar-H); a singlet at δ 6.62 (s, 1H, C^5H); a doublet at δ 4.17–4.19 (J = 10, 1H, C^8H); a double doublet at δ 3.92–4.04 (2H, SCH_2); a double doublet at δ 2.93–3.00 (1H, C^7H); a doublet at δ 2.50–2.54 (1H, C^7H); a singlet at δ 2.33 (3H, $COCH_3$); a singlet at δ 2.28 (3H, CH_3 at C-1); a singlet at δ 1.88 (3H, CH_3 at C-6) ppm.

3.2. Single X-ray diffraction studies

3.2.1. Crystal structure of III

The molecule has a cup-shaped structure, with the dihydroisoquinoline part at the base and the phenyl and carbonyl groups on the sides. A puckering analysis (Cremer and Pople, 1975) of the C3···C8 ring gave the parameters Q = 0.3386(13) Å, θ = 116.8(2)° and φ = 30.1(2)°. The dihedral angle between the mean planes of the N1/C1/C2/C3/C8/C9 and the C12···C17 rings is 83.58(2)° while the plane defined by C19/C20/C21/O1 is inclined to the N1/C1/C2/C3/C8/C9 plane by 76.39(5)°. In the crystal, C16—H16···N2 and C19—H19B···N2 hydrogen bonds plus C11—C11B···*Cg*3 interactions (Table 2) form corrugated layers of molecules parallel to the *bc* plane (Fig. 2). The layers pack along the *a*-axis direction with normal van der Waals contacts (Fig. 3).

3.2.2. Crystal structure of IV

The conformation of the substituent on sulfur is primarily determined by the N3—H3···N1 hydrogen bond and to a lesser extent by a weak C26—H26···O1 interaction (Table 3). The heterocyclic ring is planar to within 0.0167(5)Å (r.m.s. deviation = 0.0111). The mean planes of the C12···C17 and C21···C26 rings are inclined to the above plane by 85.26(3) and 36.71(3)°, respectively. A puckering analysis (Cremer and Pople, 1975) of the C3···C8 ring gave the parameters Q = 0.3738(11) Å, θ = 114.92(17)° and φ = 29.77(18)°. In the crystal, C19—H19A···O1 hydrogen bonds form inversion dimers which are connected into ribbons parallel to (024) by C7—H7···N2 hydrogen bonds and C19—H19B···*Cg*4 interactions (Table 3 and Fig. 4). The ribbons are associated through C24—H24···*Cg*3 interactions (Table 3 and Fig. 5).

3.3. Hirshfeld surface analysis

The Hirshfeld surface (HS) and two-dimensional fingerprint plots are fundamental graphical representations for measuring and displaying intermolecular interactions in a crystal structure. HS was constructed for a molecule in a crystal environment and maps various properties, including de (distance from the HS to the nearest atom outside the surface), d_i (distance from the HS to the nearest atom inside the surface), and dnorm (distance from the HS to the nearest atom inside the surface) (normalized contact distance). To gain quantitative insight into the relative contributions of the intermolecular interactions in the crystal phase, the 3-D Hirshfeld surfaces including d_{norm}, d_i, d_e, and shape index with their 2D fingerprint plots were calculated using the CrystalExplorer 14.1 software at the B3LYP/6–31 + G(d,p)level. In the 3-D maps obtained, the red regions represent closer contacts with a negative d_{norm} value while the blue regions represent longer contacts with a positive d_{norm} value. The volume of molecule **III** is 486.58 $Å^3$ and its surface area is 399.90 $Å^2$ with the corresponding values for **IV** being 534.83 $Å^3$ and 461.73 $Å^2$. The calculated Hirshfeld surface parameters are given in Table 4.

The 2-D fingerprint images provide us with information about the type of intermolecular contact between atoms and their crucial interactions between the elements which are shown in Fig. 6. Two-dimensional fingerprint plots show the proportion of the molecule's total surface area that is contributed by intermolecular inter-

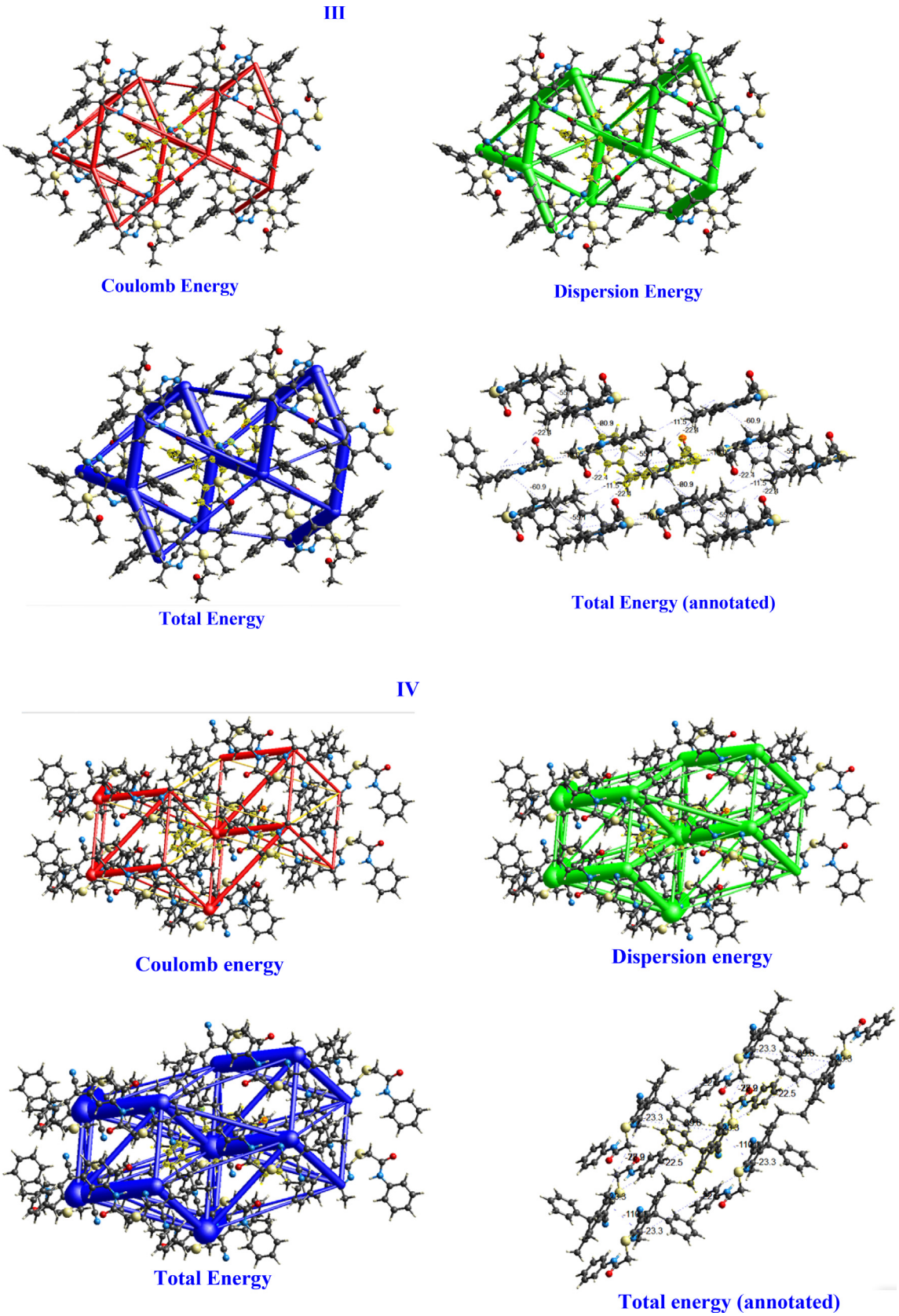

Fig. 7. Graphical representation of the interaction energies; coulomb energy, dispersion energy, and total energy for **III** and **IV.**

Table 6
The interaction energies of the molecular pairs involved in energy calculation in kJ/mol. R is the distance between molecular centroids in Å and N is the number of molecular pairs involved.

Compound (III)								
	N	Symop	R	E_ele	E_pol	E_dis	E_rep	E_tot
	1	-x, -y, -z	10.48	2.7	−1.3	−18.9	4.5	−11.5
	1	-x, -y, -z	6.08	−21.5	−9.2	−71.3	38.5	−60.9
	2	x + 1/2, -y + 1/2, z + 1/2	9.48	−8.4	−4.6	-22.0	11.1	-22.4
	2	x + 1/2, -y + 1/2, z + 1/2	12.14	−4.1	−0.8	−2.2	0.0	−6.8
	2	x + 1/2, -y + 1/2, z + 1/2	10.08	0.8	−1.0	−15.1	5.6	−8.9
	2	-x + 1/2, y + 1/2, -z + 1/2	7.71	−25.8	−7.1	−55.8	32.1	−55.1
	2	x, y, z	12.93	−3.8	−0.7	−4.2	0.0	−8.2
	1	-x, -y, -z	12.38	−9.9	−0.4	−11.1	0.0	−20.3
	2	-x + 1/2, y + 1/2, -z + 1/2	11.92	−16.3	−5.5	−9.4	11.9	−19.0
	1	-x, -y, -z	11.31	−20.5	−6.2	−11.6	10.1	−27.2
	2	x, y, z	8.80	−12.3	−5.7	−19.3	12.7	-23.3
	1	-x, -y, -z	5.18	−51.5	−13.0	−111.0	62.7	−110.1
	1	-x, -y, -z	13.96	3.0	−1.6	−15.3	0.0	−11.7
	1	-x, -y, -z	13.93	−8.1	−0.7	−4.9	0.0	−13.1
	2	x, y, z	13.17	5.8	−2.3	−29.8	0.0	-22.5
	1	-x, -y, -z	8.12	−30.0	−9.2	−82.7	39.7	−78.9
	1	-x, -y, -z	10.93	7.6	−2.0	−35.4	16.7	−12.0
	1	-x, -y, -z	8.20	−12.9	−4.4	−50.1	26.6	−39.6
	2	x, y, z	14.50	−4.2	−2.0	−8.2	0.0	−13.0
	1	-x, -y, -z	8.27	−0.5	−2.5	−21.7	9.7	−13.8

Energy Model	k_ele	k_pol	k_disp	k_rep
CE-HF ... HF/3-21G electron densities	1.019	0.651	0.901	0.811
CE-B3LYP ... B3LYP/6-31G(d,p) electron densities	1.057	0.740	0.871	0.618

actions. For **III**, the two-dimensional fingerprint results suggest that the intermolecular H···all-other-atoms contacts have the highest contribution (70.1%) to the crystal packing of which the H···H interactions contribute 51.4 %. The inside to outside H···H interactions contribute 7.3 % with the inside atom to out (neighbor fragments) interactions given in Table 5. Similarly, in **IV** intermolecular H···H interactions contribute the most (44.3%) to the crystal packing. In **III,** the relative percentage contribution of the H···all-atoms, H···H, and N···H contacts are 70.1%, 51.4%, and 7.3%, respectively.

3.4. Energy framework analysis

Energy frameworks are employed to express the interaction energies between molecular pairs in crystal packaging in crystal structures. This analysis is carried out utilizing the B3LYP functional and the 6–31 + G(d,p) basis set with the CrystalExplorer 17.5 software. The energy frameworks for molecules within 3,8 Å of a central molecule are calculated. The fragments are connected by cylinders whose thickness indicates the amount of interaction energy. The chemical pairs used to calculate interaction energies are displayed in red, blue, and green, respectively. The energy frameworks generated for Coulomb, dispersion, and total energy are represented by various colors and cylinders connecting the center of mass of the molecules with a cut-off energy of 5 kJ mol^{-1}. The size of the cylinder indicates the intensity of the forces between the molecules. Fig. 7 provides a graphical representation of the energy frameworks for **III** and **IV**, while Table 6 presents the values.

Table 7
The point group symmetry, dipole moment (in Debye), total electronic energy (in Hartree), thermal energy (in kcal/mol), Heat capacity (C_v in cal/mol K), Entropy (S in cal/mol K) energy if HOMO and LUMO (in eV), HOMO- LUMO gap (in eV), NBO chargers (Q in |e|), ionization potential (IP in Ev), electron affinity (eV), chemical hardness (Η in eV), chemical potential (eV), electronegativity (χ in eV), electrophilicity index (ω in eV), maximum charge transfer (ΔN_{max} eV)polarizability (α_o in au), hyperpolarizability (β_o in au), and projection of hyperpolarizability on dipole moment vector (β_{vec} in au).

Compound	III	IV
Point Group	C1	C1
Dipole moment (μ_o)	7.225	9.781
Energy (Hartree)	−1395.25	−1642.38
Imaginary frequency	0	0
Thermal energy (kcal/mol)	239.80	287.30
Heat capacity (C_v)	90.22	106.92
Entropy (S)	171.14	190.37
E(HOMO)	−6.26	−6.22
E(LUMO)	−2.01	−2.35
E_{H-L}	4.25	3.91
Q(O/N/S)	−0.54/-0.50/ 0.34	−0.61/-0.64/ 0.33
Ionization potential (IP)	6.26	6.22
Electron affinity (EA)	2.01	2.35
Chemical hardness (Η)	2.12	1.93
Chemical potential (μ)	−4.13	−4.28
Electronegativity (χ)	4.13	4.28
Electrophilicity index (ω)	4.02	4.74
Maximum charge transfer (ΔN_{max})	1.94	2.21
Polarizability (α_o)	288.93	361.82
Polarizability volume (α_v)	42.81	53.61
Hyperpolarizability (β_o)	415.83	488.94
Projection of hyperpolarizability (β_{vec})	408.98	476.12

3.5. DFT studies

3.5.1. Optimized geometries and electronic properties

Both molecule **III** and molecule **IV** have non-planar geometries and C1 point group symmetry. The total electronic energy for compound **III** is −1395.25 Hartree, while the slightly higher value for compound **IV** (-1642.38 Hartree) indicates that IV is more stable than **III**. Calculated dipole moments, such as 7.225 Debye for **III** and 9.78 Debye for **IV**, are used for determining the overall polarity of organic molecules (Table 7). The significant μ_o values indicate their asymmetric charge distribution and higher polarity. These structures are stable on the potential energy surface (PES) because there is no imaginary frequency associated with them. Comparing **III** and **IV**, **III** has a lower thermal energy at 239.804 kcal/mol, whereas IV has a higher thermal energy at 287.304 kcal/mol.

3.5.2. FMOs and NBO studies

The relative positions of a molecule's most crucial Frontier Molecular Orbitals (FMOs), typically the highest occupied molecular orbital (HOMO) and the lowest unoccupied molecular orbital (LUMO), determine the molecule's chemical stability (Fig. 8). Donating electrons is related to the HOMO state while gaining them is linked to the LUMO state. A compound's electrophilic nature is indicated by its ELUMO value, whereas its nucleophilic strength is measured by its EHOMO value. The calculated energies of the HOMOs for **IV** and **III** are −6.26 and −6.22 Ev, respectively (Table 7) while the computed HOMO-LUMO gaps (E_{H-L}) for **III** and **IV** are 4.25 and 3.91 eV, respectively. The relatively small E_{H-L} gaps suggest the molecules are "soft" and so may be susceptible to oxidation and likely fairly reactive in other respects.

Understanding the atomic charge of a chemical system is greatly enhanced by NBO analysis. The calculated NBO charges are listed in Table 7. The natural atomic orbitals (NAOs) of the atoms can be added up to determine their partial charges during an NBO analysis. Predicting the dipole moment and molecular polarisations are just two examples of the many quantum features of molecular systems that can be inferred from the charges. NBO charge analysis can also be used to gain knowledge about donor–acceptor pairings and charge transfer within a molecule. Table 6 displays the obtained NBO charges. The partial NBO charges on the oxygen atom in **III** and **IV** are −0.54 |e| and −0.61 |e|. The presence of negative NBO charges throughout the oxygen atom denotes its donor potential. Electrophilic attack on oxygen and nitrogen atoms in compound **III** allows for the further derivation of the process. Compound **III**, on the other hand, exhibits nucleophilic addition reactivity at its S-atom. The higher electronegativity of the oxygen atom pulls the electrons of adjacent carbon and makes it partially positive (a good electrophilic center). Therefore, charge transfer can be seen from an electropositive to a more electronegative atom which indicates structural reactivity and binding affinity. The hydrogen atoms attached to the carbons of the central rings have partial positive NBO charges. In **IV,** the NBO charge at oxygen Q(O) is higher (more negative) than that in **III**. The calculated NBO charges on Q(O), Q(N), and Q(S) are −0.61, −0.64, and 0.33 |e|, respectively (Table 7). The excellent charge separation and transfer of charge show higher structural reactivity of **III** and **IV**.

3.5.3. MESP and DOS study

The MEP is a measure of the net electrostatic impact created at a specific location by the total charge distribution (electron + proton) of the molecule, and can be used to infer the dipole moment, electro negativity, partial charges, and chemical reactivity of a molecule. An electron density isosurface mapped with an electrostatic potential surface depicts the molecules' dimensions, shapes, charges, and places of chemical reaction (see Fig. 9). For **III,** the highest electronic density (high electron site) can be seen near the carbonyl oxygen and around the nitrogen of the central pyridine ring. The red color shows the possibility of an electrophilic attack on this position for further reactions. The red color represents the minimum electrostatic potential (high electron density) with a negative electrostatic potential, serving as an electrophilic attack region for the substances being investigated. The zero electrostatic potential zone, on the other hand, is represented by the green color. Thus, the numerous zones of MESP plots reveal critical information about the various types of intermolecular interactions, allowing them to predict the reactivity of the molecule. Compound **IV** also has an electron-rich area close to its nitrogen and oxygen atoms but with a lesser magnitude suggesting a similar but lesser reactivity.Fig. 10.

The energy gap determined by HOMO-LUMO analysis is supported by the DOS spectrum. The DOS spectra are displayed as energy against state density. Reduced HOMO-LUMO gaps are due to the generation of higher HOMO energy states. The higher energy of occupied orbitals allows electrons to be transferred from HOMO to LUMO. As a result of the small energy gaps, compounds III and IV have a soft nature and better semiconducting characteristics. The HOMO energy line is near −5.44 eV, whereas the LUMO energy decreases, indicating their usefulness in the fabrication of electrical and optical materials.

3.5.4. Electronic stability and global reactivity descriptor

To better comprehend the reactivity and structural properties, the global reactivity descriptors as ionization potential (IP), electron affinity (EA), chemical hardness (η), chemical potential (μ), electronegativity (χ), maximum charge transfer (ΔN_{max}), and electrophilicity index (ω) we calculated as indicated by the following equations;

Ionization potential (IP) = − E (HOMO)

Electron affinity (EA) = − E (LUMO)

Quantum chemical Hardness (η) = ½ (IP- EA)

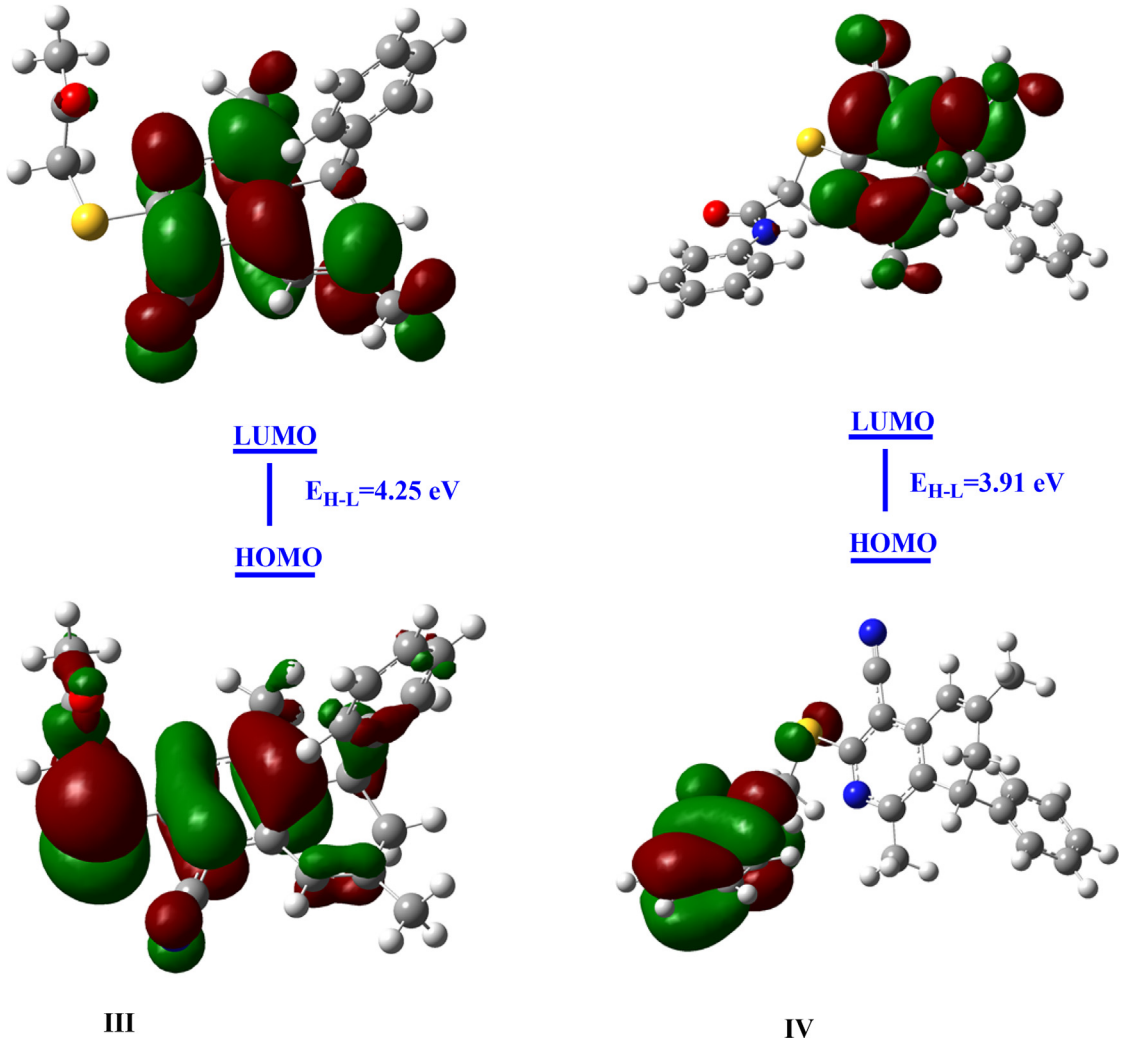

Fig. 8. Plotted HOMO-LUMO densities of **III** and **IV** at the B3LYP level.

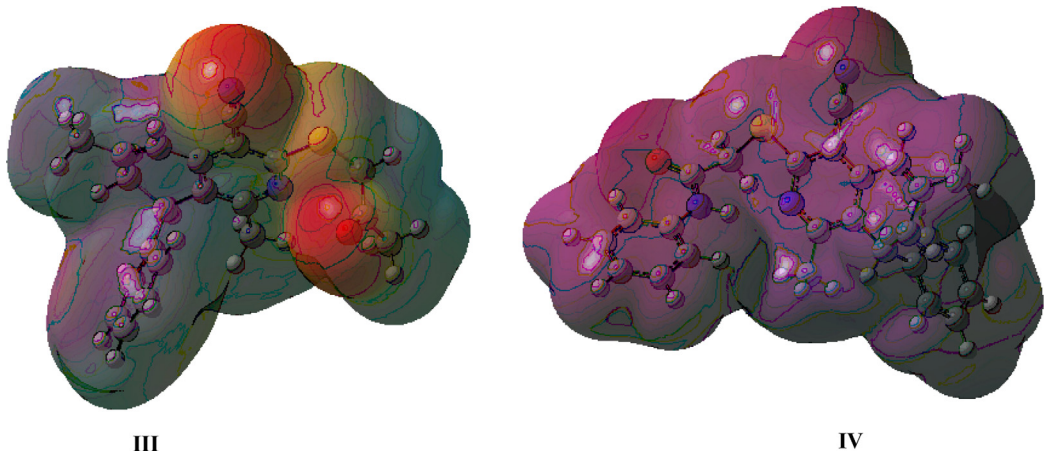

Fig. 9. MESP surfaces of III and IV at B3LYP.

Chemical potential (μ) = $-\frac{IP+EA}{2}$
Electronegativity (χ) = $-\mu$
Electrophilicity index (ω) = $\frac{\mu^2}{2\eta}$

The maximum charge transfer (ΔN_{max}) in the direction of the electrophile of the molecule was predicted using the following.

$$\Delta N_{max} = -\frac{\mu}{\eta}$$

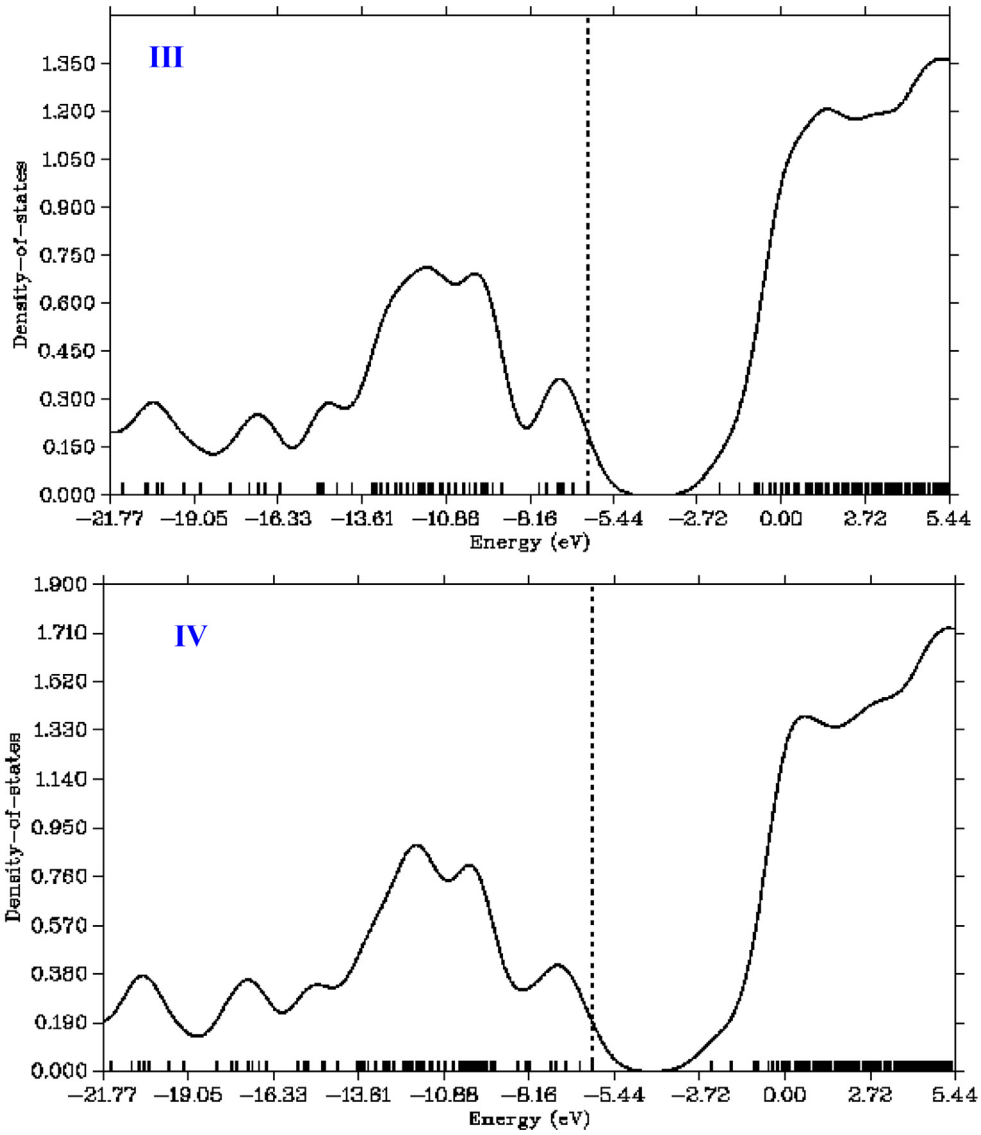

Fig. 10. TDOS spectra of compounds (III and IV).

Table 8
Illustrates the docking score and glide energy of different small molecules.

Compound	Docking score (kcal/mol)	Glide energy (kcal/mol)
III	−6.971	−47.115
IV	−6.403	−47.242
Native ligand molecule (YCM)	−5.741	−37.270

The ionization potential (IP) and electron affinity (EA) are calculated using Koopman's approximations, with IP standing in for the inverse of the HOMO and EA for the inverse of the LUMO. The calculated ionization potentials for **III** and **IV** are 6.26 and 6.22 eV (Table 7) which indicate their electronic stability. The calculated electron affinity (Table 7) for **IV** is somewhat greater than that of **III** while **IV** is "softer" than **III** from the computed chemical hardness. The negative of the Mulliken electronegativity is the chemical potential (μ). It is a signal that a chemical reaction is about to occur. This means that a high electronic chemical potential reagent is a strong electron donor, whereas a low electronic chemical potential reagent is a good electron acceptor. The chemical potential (μ) for **III** and **IV** are, respectively −4.13 to −4.28 eV and have comparable values. On the other hand, the electronegativities (χ) are 4.13 and 4.28 eV. Another parameter to classify the molecular reactivity is maximum charge transfer (ΔN_{max}) which can be defined as; the propensity of a molecular system to acquire an additional electronic charge. For the studied molecules, the inhibitor efficiency is also calculated using the maximal charge transfer ΔN_{max}. The values of ΔN_{max} show the bearing within a set of molecules and the highest value of ΔN_{max} is associated with high inhibitor efficiency. The value of ΔN_{max} is higher for compound **IV** while for compound **III** slightly smaller.

3.5.5. Optical and nonlinear optical (NLO) properties

By calculating the polarizability (αo), hyperpolarizability (βo), and the projection of hyperpolarizability on the dipole moment vector (βvec), the optical and nonlinear optical properties of **III** and **IV** were investigated. The conjugated structures that make up organic non-linear optical materials allow π-electrons to readily move between donor and acceptor groups, facilitating charge transfer and resulting in a response time that is many times faster than that of inorganic materials. The coefficients in the Taylor series expansion of the energy in the external electric field constitute

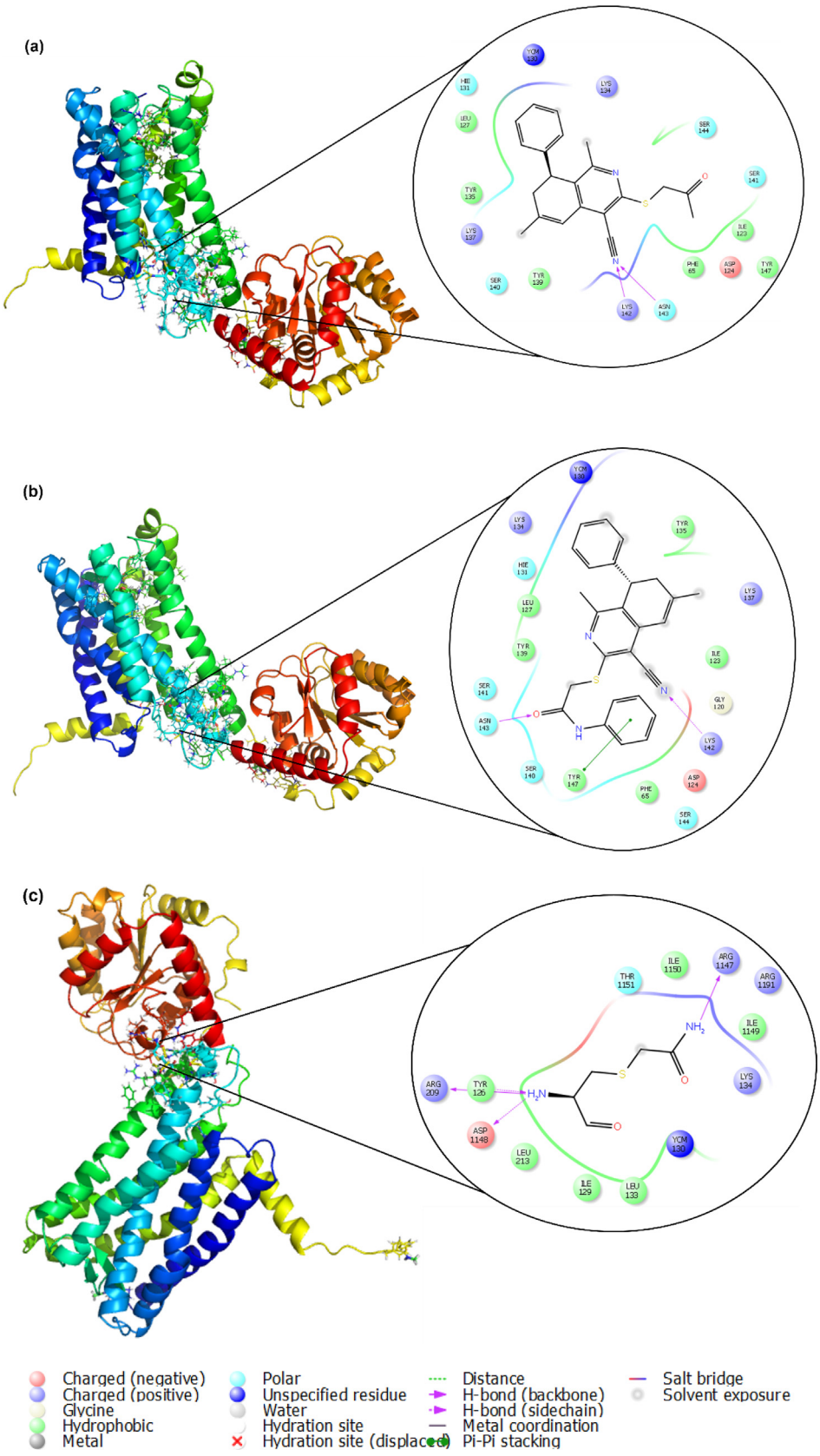

Fig. 11. Best Docked posed of the protein–ligand complex and its corresponding ligand plot (a) with **III**, (b) with **IV,** and (c) with YCM (native ligand).

Table 9
Predicted "drug-like" properties and estimated properties of absorption and distribution of compounds **III** and **IV.**

Compound	Drug Likeness	Solubility	ABS	Absorption & distribution								
	MW	WlogP	HBA	HBD	TPSA Å²	Nrot	Class (ESOL)		WlogP	GIA	Pgp	BBB
III	**348.46**	**2.84**	**3**	**0**	**79.05**	**4**	**Moderate**	**0.55**	**4.77**	**High**	**No**	**No**
IV	**425.55**	**3.51**	**3**	**1**	**91.08**	**6**	**Moderate**	**0.55**	**5.63**	**High**	**Yes**	**No**

Drug lead like properties ideal values ≤ 500 (MW) ≤ 4.15(MlogP) ≤ 10(HBA) ≤ 5 (HBD) ≤ 142(TSPSA) ≤ 10(Nrot).

the components of β. When the external electric field is weak and homogeneous, this expansion becomes:

$$E = E^{O} - \mu_i F_i - \left[\frac{1}{2!}\right]\alpha_{ij}F_iF_j - \frac{1}{3!}\beta_{ijk}F_iF_jF_k - [\frac{1}{4!}]\gamma_{ijkl}F_iF_jF_kF_l$$

The polarizability (α_o) and static hyperpolarizability (β_o) are given by the following equations;

$$\alpha_o = \frac{1}{3}(\alpha xx + \alpha yy + \alpha zz)$$

$$\beta_o = \sqrt{(\beta^2{}_x + \beta^2{}_Y + \beta^2{}_Z)}$$

The calculated polarizability (α_o) value of **III** is 288.93 au while that of **IV** is 361.82 au (Table 6). These substantial values suggest the polarizability of molecules and asymmetric charge distribution. As with the α_o values, the β_o value for **IV** (488.94 au) is slightly higher than that of **III** (415.83 au). These results indicate that **III** and **IV** have good NLO properties and are potential candidates for further development.

3.6. Molecular docking study

The simulation of molecular docking generates multiple possible poses from which we have to choose the optimal one based on glide energy and docking score (Abad et al., 2022; Abdel-Rahman et al., 2021; El Bakri et al., 2023a, 2023b, 2022, 2019; Mohamed et al., 2022). Each ligand molecule was designed to interact with its respective protein's native ligand site. Table 8 represents the ligand molecules and their corresponding docking score and glide energy. The binding score of different drugs shows good binding affinity towards the protein structure.

Fig. 11 represents the best-docked pose and its corresponding ligand interaction plot. In Fig. 11**a**, the interaction of compound **III** with the protein shows that LEU 127, TYR 135, TYR 139, PHE 65, ILE 123, TYR 147 residues are forming hydrophobic interactions and, LYS 142, ASN 143 residues are forming hydrogen bonds with the C≡N group of the compound **III** due to the presence of lone pair of electrons on the nitrogen atom.

Similarly, the ligand interaction plot for compound **IV** is shown in Fig. 11b. LEU 127, TYR 139, PHE 65, ILE 123, and TYR 135 residues interact hydrophobically. Although TYR 147 is a hydrophobic residue it forms pi-pi stacking with the aromatic part of the ligand. YCM is the native site of the protein structure. ASN 143 and LYS 142 form hydrogen bonds with C = O and C≡N groups of **IV**. Here, LYS 134, LYS 142, and LYS 137 are positively charged residues, and HIE 131, SER 141, ASN 143, SER 140, and SER 144 are polar residues.

In this work, the native ligand molecule YCM was extracted from the protein structure separately and docked in the same native site. Fig. 11c shows the best-docked pose of the native molecule and its corresponding ligand plot. YCM native ligand has more hydrogen bond contacts compared to the other two compounds. TYR 126 forms hydrogen bonds with the $-NH_2$ of the ligand and the ARG 209 residue and $-NH_2$ interacts with ASP 1148 through hydrogen bonding. Similarly, the other $-NH_2$ forms a hydrogen bond with ARG 1147. TYR 126, LEU 213, ILE 129, LEU 133, ILE 1150, and ILE 1149 are hydrophobic residues and THR 1151 is the polar residue. ASP 1148 is negatively charged while others are positively charged.

This study concludes that all the ligand molecules have good binding affinities at the molecular level and all three molecules have more hydrophobic contacts in the protein environment.

3.7. ADMET analysis

The Brain or Intestinal EstimateD permeation (BOILED-Egg), which was derived from Egan's multi-statistical graph model (Egan et al., 2000; Silva et al., 2021), employs mathematical descriptors of lipophilicity (WlogP) and polarity (TPSA) to predict human intestinal absorption (HIA) and access to the central nervous system (CNS) by breaching the blood–brain barrier (BBB. Therefore, the ellipse formed by the intersection of the lipophilicity and polarity profiles accounts for substances that are both highly and inadequately absorbed in the human gut and have a linear trend. Table 9 shows the limits of WlogP between 4 and 6 and for compound, **III** TPSA is less than 79, from these results this compound may have connected to CNS assess, In the case of compound **IV**, the TSPSA which is garter than 79, and which leads high HIA. Both compounds exhibit drug-likeness properties and show better polarity, lipophilicity, and bioavailability.

According to the information in Table S5, both substances block all CY450 isoenzymes except for CY450 1A2 & 2D6, which may cause their plasma concentration to rise and the elimination pathway to slow down. It is also metabolized by O-demethylation pathways, reducing the danger of liver damage brought on by metabolic activation, as neither molecule is an inhibitor of CYP450 2D6. Additionally, as shown in Table S5, both compounds have a class IV toxicity when taken with projected LD50 values of 600 mg/kg and an immunotoxic risk with a prediction accuracy of 54%. The overall result concludes that both compounds exhibit better ADMET properties.

4. Conclusion

To sum up, a new dihydroisoquinoline derivatives were synthetized and confirmed by single-crystal X-ray analysis. Hirshfeld surface analysis displays 2D fingerprint plots with a predominance of H···H surface contacts to identify intermolecular interactions. The shown dnorm and di surfaces as well as the 2-D fingerprint plots reveal short and long intermolecular interactions. The interaction energies between chemical pairs in crystal structures are revealed as well via energy framework analysis. The two compounds' electronic stability and reactivity are demonstrated by the DFT study. The HOMO-LUMO and global reactivity characteristics indicate that **IV** has a higher chemical reactivity than does **III**. The HOMO-LUMO gaps are 4.25 and 3.91 Ev. A maximum charge transfer (ΔN_{max}) value of 2.21 eV is observed for **IV**. The estimated polarizability (α_o) and hyperpolarizability (β_o) responses were used to determine their optical and nonlinear optical properties.

The large β_o value (488.94 au) for **IV** reveals its optical and NLO characteristics. When compared to the original molecule, **III** and **IV** used to investigate the docking with human melatonin receptors 1 showed good binding scores. Additionally, an ADMET study was carried out and the outcomes point to both **III** and **IV** having better ADMET qualities.

Funding

This research was funded by Researchers Supporting Project No. RSP-2023R353, King Saud University, Riyadh, Saudi Arabia.

Declaration of competing interest

The authors declare that they have no known competing financial interests or personal relationships that could have appeared to influence the work reported in this paper.

Acknowledgement

The authors extend their appreciation to the Researchers Supporting Project, King Saud University, Riyadh, Saudi Arabia, for funding this work through grant No. RSP-2023R353.

Appendix A. Supplementary data

Supplementary data to this article can be found online at https://doi.org/10.1016/j.arabjc.2023.105294.

References

Abad, N., El Bakri, Y., Lai, C.-H., Karthikeyan, S., Ramli, Y., Ferfra, S., Mague, J.T., Essassi, E.M., 2022. Insights into the crystal structure of two newly synthesized quinoxalines derivatives as potent inhibitor for c-Jun N-terminal kinases. J. Biomol. Struct. Dyn. 40, 2797–2814.

Abdel-Rahman, L.H., Mohamed, S.K., El Bakri, Y., Ahmad, S., Lai, C.-H., Amer, A.A., Mague, J.T., Abdalla, E.M., 2021. Synthesis, crystal structural determination and in silco biological studies of 3, 3′-ethane-1, 2-diylbis (2-benzylidene-1, 3-thiazolidin-4-one. J. Mol. Struct. 1245, 130997.

Adamah-Biassi, E.B., Zhang, Y., Jung, H., Vissapragada, S., Miller, R.J., Dubocovich, M. L., 2014. Distribution of MT1 melatonin receptor promoter-driven RFP expression in the brains of BAC C3H/HeN transgenic mice. J. Histochem. Cytochem. 62, 70–84.

Albert, A., Rubbo, S.D., Goldacre, R.J., Balfour, B.G., 1947. The influence of chemical constitution on antibacterial activity. Part III: A study of 8-hydroxyquinoline (oxine) and related compounds. Br. J. Exp. Pathol. 28, 69.

Al-Ghoul, W.M., Herman, M.D., Dubocovich, M.L., 1998. Melatonin receptor subtype expression in human cerebellum. Neuroreport 9, 4063–4068.

Anary-Abbasinejad, M., Anaraki-Ardakani, H., Mosslemin, M.H., Khavasi, H.R., 2010. Isoquinoline-catalyzed reaction between 4-hydroxycoumarin or 4-hydroxy-6-methylpyran-1-one and dialkyl acetylene dicarboxylates: synthesis of coumarin and pyranopyrane derivatives. J. Braz. Chem. Soc. 21, 319–323.

Asghari, S., Malekian, N., Esmaeilpour, R., Ahmadipour, M., Mohseni, M., 2014. Three-component synthesis and antibacterial evaluation of some novel 1, 2-dihydroisoquinoline derivatives. Chinese Chem. Lett. 25, 1441–1444.

Audinot, V., Mailliet, F., Lahaye-Brasseur, C., Bonnaud, A., Le Gall, A., Amossé, C., Dromaint, S., Rodriguez, M., Nagel, N., Galizzi, J.-P., 2003. New selective ligands of human cloned melatonin MT 1 and MT 2 receptors. Naunyn Schmiedebergs Arch. Pharmacol. 367, 553–561.

Bruker (2016), 2016. APEX3, SAINT and SADABS. Bruker AXS Inc., Madison, Wisconsin, USA. 2014.

Bruker. APEX3, SADABS, SAINT and SHELXTL. Bruker AXS Inc., Madison, Wisconsin, USA., 2016.

Burley, S.K., Bhikadiya, C., Bi, C., Bittrich, S., Chen, L., Crichlow, G.V., Christie, C.H., Dalenberg, K., Di Costanzo, L., Duarte, J.M., Dutta, S., Feng, Z., Ganesan, S., Goodsell, D.S., Ghosh, S., Green, R.K., Guranovic, V., Guzenko, D., Hudson, B.P., Lawson, C.L., Liang, Y., Lowe, R., Namkoong, H., Peisach, E., Persikova, I., Randle, C., Rose, A., Rose, Y., Sali, A., Segura, J., Sekharan, M., Shao, C., Tao, Y.P., Voigt, M., Westbrook, J.D., Young, J.Y., Zardecki, C., Zhuravleva, M., 2021. RCSB Protein Data Bank: Powerful new tools for exploring 3D structures of biological macromolecules for basic and applied research and education in fundamental biology, biomedicine, biotechnology, bioengineering and energy sciences. Nucleic Acids Res. 49, D437–D451. https://doi.org/10.1093/nar/gkaa1038.

Caricato, M., Frisch, M.J., Hiscocks, J., Frisch, M.J., 2009. Gaussian 09: IOps Reference. Gaussian.

Collery, P., Lechenault, F., Cazabat, A., Juvin, E., Khassanova, L., Evangelou, A., Keppler, B., 2000. Inhibitory effects of gallium chloride and tris (8-quinolinolato) gallium III on A549 human malignant cell line. Anticancer Res 20, 955–958.

Cremer, D.t., Pople, J.A., 1975. General definition of ring puckering coordinates. J. Am. Chem. Soc. 97, 1354–1358.

Dennington, R., Keith, T., Millam, J., 2009. GaussView.

Domingo, L.R., Ríos-Gutiérrez, M., Pérez, P., 2016. Applications of the conceptual density functional theory indices to organic chemistry reactivity. Molecules 21, 748.

Dubocovich, M.L., Delagrange, P., Krause, D.N., Sugden, D., Cardinali, D.P., Olcese, J., 2010. International Union of Basic and Clinical Pharmacology. LXXV. Nomenclature, classification, and pharmacology of G protein-coupled melatonin receptors. Pharmacol. Rev. 62, 343–380.

Egan, W.J., Merz, K.M., Baldwin, J.J., 2000. Prediction of drug absorption using multivariate statistics. J. Med. Chem. 43, 3867–3877.

El Bakri, Y., Marmouzi, I., El Jemli, M., Anouar, E.H., Karthikeyan, S., Harmaoui, A., Faouzi, M.E.A., Mague, J.T., Essassi, E.M., 2019. Synthesis, biological activity and molecular modeling of a new series of condensed 1,2,4-triazoles. Bioorg. Chem. 92. https://doi.org/10.1016/j.bioorg.2019.103193.

El Bakri, Y., Kurbanova, M.M., Siddique, S.A., Ahmad, S., Goumri-Said, S., 2022. One-pot synthesis, X-ray crystal structure, and identification of potential molecules against COVID-19 main protease through structure-guided modeling and simulation approach. Arab. J. Chem. 15, 104230.

El Bakri, Y., Kurbanova, M., Ahsin, A., Ramazanzade, N., Al-Salahi, R., 2023a. A probe to surface reactivity, crystal structure, and DFT investigations for newly synthesized 4,5-bis(4-nitrophenyl)-8a-phenyl-decahydro-[1,3]diazino[4,5-d] pyrimidine-2,7-dione: a combined theoretical and experimental study. Crystals. https://doi.org/10.3390/cryst13060942.

El Bakri, Y., Kurbanova, M., Siddique, S.A., Karthikeyan, S., Maharramov, A., Ramazanzade, N., 2023b. Synthesis, virtual screening, and computational approach of 6-(4-metoxyphenyl)-4-phenyl-1, 2-dihydropyrimidin-2-one as a potential target for thioredoxin glutathione reductase (TGR). J. Mol. Struct. 135623

Khaleghi, F., Din, L.B., Jantan, I., Yaacob, W.A., Khalilzadeh, M.A., 2011. A facile synthesis of novel 1, 4-benzoxazepin-2-one derivatives. Tetrahedron Lett. 52, 7182–7184.

Liu, C., Weaver, D.R., Jin, X., Shearman, L.P., Pieschl, R.L., Gribkoff, V.K., Reppert, S.M., 1997. Molecular dissection of two distinct actions of melatonin on the suprachiasmatic circadian clock. Neuron 19, 91–102.

Lukevics, E., Segal, I., Zablotskaya, A., Germane, S., 1997. Synthesis and neurotropic activity of novel quinoline derivatives. Molecules 2, 180–185.

Mazzucchelli, C., Pannacci, M., Nonno, R., Lucini, V., Fraschini, F., Stankov, B.M., 1996. The melatonin receptor in the human brain: cloning experiments and distribution studies. Mol. Brain Res. 39, 117–126.

Mohamed, S.K., El, Y., Abdul, D.A., Ahmad, S., Albayati, M.R., Lai, C., Mague, J.T., Tolba, M.S., 2022. Synthesis, crystal structure, and a molecular modeling approach to identify effective antiviral hydrazide derivative against the main protease of SARS-CoV-2. J. Mol. Struct. 1265,. https://doi.org/10.1016/j.molstruc.2022.133391 133391.

Nassiri, M., Maghsoodlou, M.T., Heydari, R., Habibi Khorassani, S.M., 2008. Novel multicomponent reactions involving isoquinoline or phenanthridine and activated acetylenic ester in the presence of heterocyclic NH or 1, 3-dicarbonyl compounds. Mol. Divers. 12, 111–117.

Reppart, S.M., Weaver, D.R., Godson, C., 1996. Melatonin receptors step into the light: cloning and classification of subtypes. Trends Pharmacol. Sci. 17, 100–102.

SAINT. Data Reduction and Correction Program.Version 8.34A.Bruker AXS Inc., Madison, Wisconsin, USA, 2014., n.d.

Scott, J.D., Williams, R.M., 2002. Chemistry and biology of the tetrahydroisoquinoline antitumor antibiotics. Chem. Rev. 102, 1669–1730.

Sheldrick, G.M., 2015. SHELXT – Integrated space-group and crystal-structure determination. Acta Crystallogr. A 71, 3–8. https://doi.org/10.1107/S2053273314026370.

Shen, A.Y., Chen, C.P., Roffler, S., 1999. A chelating agent possessing cytotoxicity and antimicrobial activity: 7-morpholinomethyl-8-hydroxyquinoline. Life Sci. 64, 813–825.

Sherman, W., Beard, H.S., Farid, R., 2006a. Use of an induced fit receptor structure in virtual screening. Chem. Biol. Drug Des. 67, 83–84. https://doi.org/10.1111/j.1747-0285.2005.00327.x.

Sherman, W., Day, T., Jacobson, M.P., Friesner, R.A., Farid, R., 2006b. Novel procedure for modeling ligand/receptor induced fit effects. J. Med. Chem. 49, 534–553. https://doi.org/10.1021/jm050540c.

Silva, J., Rocha, M.N.d., Marinho, E.M., Marinho, M.M., Marinho, E.S., Santos, H.S.d., 2021. Evaluation of the ADME, toxicological analysis and molecular docking studies of the anacardic acid derivatives with potential antibacterial effects against staphylococcus aureus. J. Anal. Pharm. Res. 10, 177–194.

Spackman, P.R., Turner, M.J., McKinnon, J.J., Wolff, S.K., Grimwood, D.J., Jayatilaka, D., Spackman, M.A., 2021. CrystalExplorer: a program for Hirshfeld surface analysis, visualization and quantitative analysis of molecular crystals. J. Appl. Crystallogr., 54

Stauch, B., Johansson, L.C., McCorvy, J.D., Patel, N., Han, G.W., Huang, X.P., Gati, C., Batyuk, A., Slocum, S.T., Ishchenko, A., Brehm, W., White, T.A., Michaelian, N., Madsen, C., Zhu, L., Grant, T.D., Grandner, J.M., Shiriaeva, A., Olsen, R.H.J., Tribo, A.R., Yous, S., Stevens, R.C., Weierstall, U., Katritch, V., Roth, B.L., Liu, W., Cherezov, V., 2019. Structural basis of ligand recognition at the human MT1

melatonin receptor. Nature 569, 284–288. https://doi.org/10.1038/s41586-019-1141-3.
Tietze, L.F., Rackelmann, N., Müller, I., 2004. Enantioselective total syntheses of the Ipecacuanha alkaloid emetine, the Alangium alkaloid tubulosine and a novel benzoquinolizidine alkaloid by using a domino process. Chem Eur J 10, 2722–2731.
Tirado-Rives, J., Jorgensen, W.L., 2008. Performance of B3LYP density functional methods for a large set of organic molecules. J. Chem. Theory Comput. 4, 297–306.
Weaver, D.R., Rivkees, S.A., Reppert, S.M., 1989. Localization and characterization of melatonin receptors in rodent brain by in vitro autoradiography. J. Neurosci. 9, 2581–2590.
Wehner, F.C., Thiel, P.G., Van Rensburg, S.J., Demasius, I.P.C., 1978. Mutagenicity to Salmonella typhimurium of some Aspergillus and Penicillium mycotoxins. Mutat. Res. Toxicol. 58, 193–203.
Yadav, J.S., Reddy, B.V., Yadav, N.N., Gupta, M.K., Sridhar, B., 2008. Gold (III) chloride-catalyzed three-component reaction: a facile synthesis of alkynyl derivatives of 1, 2-dihydroquinolines and isoquinolines. J. Org. Chem. 73, 6857–6859.
Yavari, I., Ghazanfarpour-Darjani, M., Sabbaghan, M., Hossaini, Z., 2007. Synthesis of dimethyl 1, 2-dihydroisoquinolines through the reaction of isoquinoline and dimethyl acetylenedicarboxylate in the presence of amides. Tetrahedron Lett. 48, 3749–3751.
Yavari, I., Piltan, M., Moradi, L., 2009. Synthesis of pyrrolo [2, 1-a] isoquinolines from activated acetylenes, benzoylnitromethanes, and isoquinoline. Tetrahedron 65, 2067–2071.
Zhao, Y., Truhlar, D.G., 2006. Density functional for spectroscopy: no long-range self-interaction error, good performance for Rydberg and charge-transfer states, and better performance on average than B3LYP for ground states. Chem. A Eur. J. 110, 13126–13130.